5

Collisional excitations and charge multiplication in uniform fields

5.1 Inelastic electron–molecule collisions

When the electric field is increased above a few kV/cm, more and more electrons can acquire enough energy between two collisions to produce inelastic phenomena, excitations of various kinds and ionizations. A molecule can have several characteristic modes of excitation, increasing in number and complexity for polyatomic molecules; typical values for the lowest excitation levels are between ten and twenty electron volts. In each collision, an electron can spend an amount of energy equal to or larger than the excitation energy; the atom or molecule, left in an excited state, returns to the ground state through single or multiple transitions.

Noble gas atoms de-excite through photon emission, while weakly bound polyatomic molecules, as for example the hydrocarbons widely used in proportional counters as a quencher, have rotational and vibrational radiationless transitions. Addition of an organic vapour to noble gases therefore allows the dissipation of a good fraction of energy without the creation of photons or ions, an important factor to permit high gain and stable operation of proportional counters.

At higher fields, the probability of ionizing collisions increases and exceeds the decreasing probability of excitations; the outcome of an ionizing collision is the creation of an electron–ion pair, while the primary electron continues its motion in the gas. When the mean free path for ionizing collisions is small compared to the gas layer thickness, the two electrons soon acquire sufficient energy from the field to ionize further; this leads to a rapid growth of an electron–ion avalanche, and constitutes the basic mechanism of signal amplification in gas proportional counters.

Examples of absolute cross sections for electron–molecule collisions as a function of electron energy were given in the previous chapter. For a given value of the field, the statistical electron energy distribution spans a range of values of the cross sections, determining the relative probability of the various processes; at high

https://doi.org/10.1017/9781009291200.007 Published online by Cambridge University Press

Table 5.1 *Major processes in electron and ion–molecule collisions; A and B designate two atoms (molecules), A*, B* their excited states and A^+, A^-, B^+ the corresponding ions.*

Process	Initial	Final
Excitation	A+e	A*+e
Ionization	A+e	A^++e+e
De-excitation	A*+e	A+e
Photo-excitation	A+hυ	A*
Photo-ionization	A+ hυ	A^++e
Photo-emission	A*	A+hυ
Electron capture	A+e	A^-
Radiative recombination	A^++e	A+hυ
Excimers formation	A*+A+A	A_2*+A
Radiative excimer dissociation	A_2*	A+A+ hυ
Collisional de-excitation	A*+B	A+B*
Charge exchange	A^++B	A+B^+
Penning effect	A*+B	A+B^++e

fields, such as those encountered in gaseous detectors, the contribution of elastic processes becomes negligible, while excitations and ionizations tend to share the spent energy almost equally.

A large number of processes can follow the inelastic interaction of electrons and molecules; more than 20 are described in Meek and Cragg (1953). Table 5.1 summarizes those having a major impact on the operation of gaseous detectors in a pure gas A and mixtures of two gases A and B. Depending on the species, the probability of a process can be very different, and not all processes are energetically permitted. The process of molecular dissociation, direct or going through a phase of pre-dissociation, which result in breaking the molecule into two or more fragments, competes with the other de-excitation mechanisms; radiationless internal conversions can also occur, relaxing the molecule into the lowest excited state of a given multiplicity. Even a superficial description of these mechanisms would be far beyond the scope of this book; the reader is referred to the textbooks quoted above and in particular Christophorou (1971) for a more detailed analysis.

5.2 Excitations and photon emission

Electronic excitation processes have been extensively studied, both theoretically and experimentally, for rare gases and their mixtures. Originally motivated by the research on gaseous discharges and by the related field of proportional counters operation, this branch of applied research has received more interest in connection with the development of excimer gas lasers, see for example Rhodes (1979). The mechanisms leading to the creation and decay of excited states in pure noble gases

https://doi.org/10.1017/9781009291200.007 Published online by Cambridge University Press

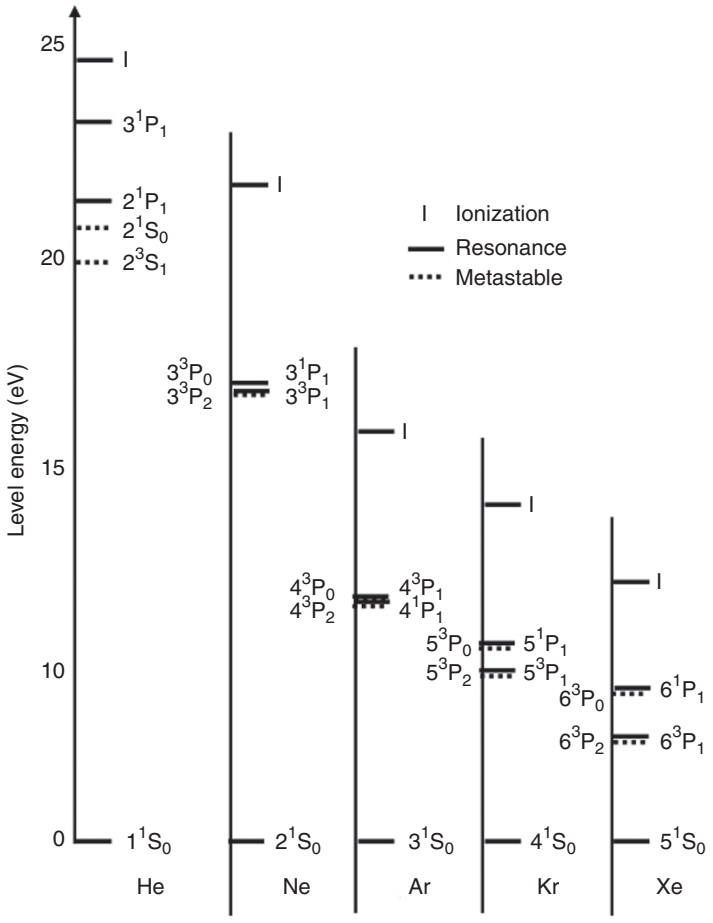

Figure 5.1 First electronic excitation and ionization levels for the noble gases (compiled from different sources).

and their mixtures are rather well understood, and quantitative calculations are possible using the appropriate formulations. This is to a much lesser extent the case for molecular gases; even for the simplest ones, such as the hydrocarbons often used in proportional counters, the study is often reduced to a purely phenomenological description of the energy exchange processes involved.

Figure 5.1, from different sources, shows schematically the lowest excitation and ionization levels for noble gases; numerical values of the corresponding energies were given in Table 2.1. Except for helium, rare gases have a very similar electronic structure, with the lowest excited states corresponding to one electron raised from the ground state $^1S_0$ to a $^1P_1$ singlet or to one of the $^3P_2$, $^3P_1$ or $^3P_0$ triplets.

Excited by electron impact, isolated noble gas atoms return to the ground state with the emission of a photon with an energy corresponding to the excitation level.

https://doi.org/10.1017/9781009291200.007 Published online by Cambridge University Press

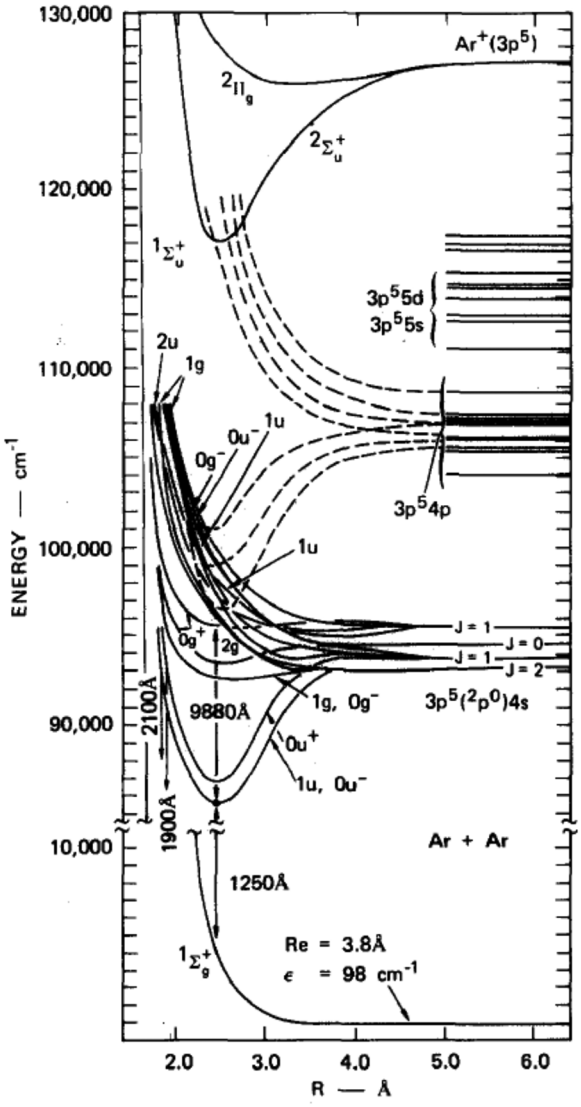

Figure 5.2 Argon excimer potential curves (Lorents, 1976). By kind permission of Elsevier.

However, at increasing pressures, collision of an excited atom with a neutral one can result in temporary formation of bound states, short-lived molecules named dimers for which lower energy transitions can occur. The energy levels of the argon dimer are shown in the Debye plot, Figure 5.2 (Lorents, 1976); the atomic levels correspond to the asymptotic values of the curves at large inter-atom separations. The atomic radiative de-excitation energy, 11.6 eV, corresponds to

https://doi.org/10.1017/9781009291200.007 Published online by Cambridge University Press

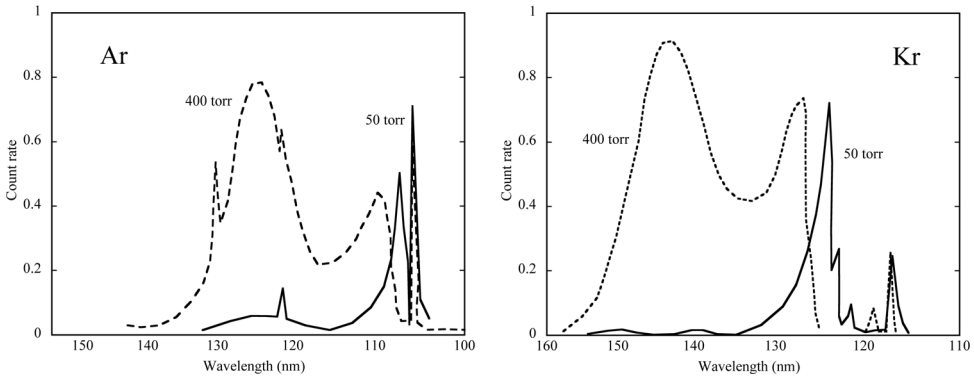

Figure 5.3 Fluorescence emission of argon and krypton excimers at different pressures (Hurst and Klots, 1976). By kind permission of John Wiley & Sons.

the emission of a photon with a corresponding wavelength (1050 Å), while the excimer emission is peaked at 1250 Å, as indicated in the figure. The relative fraction of dimeric and atomic emission depends on pressure, with the longer wavelength emission dominating above a few hundred torr, as shown in Figure 5.3 for argon and xenon (Hurst and Klots, 1976).

The creation of excited states by electron or particle impact and their successive evolution into radiative levels of the excimers is a very complex process; the timing properties of the emitted radiation depend both on the formation time, i.e. the time it takes for the excited states to form the diatomic molecules, and on the subsequent decay time to the ground state. For a review of the rare gases luminescence processes see for example Salete Leite (1980).

The photon emission increases rapidly with the applied electric field due to the increasing number of electrons with energy above the excitation level, and to the onset of charge multiplication. All gases emit photons when excited by electron impacts; however, the yields vary in a wide range, and depend on the wavelength sensitivity range covered by the detection method. As an example, Figure 5.4 shows the relative luminescence yields of a proportional counter measured in several gases as a function of the anode voltage (Keirim-Markus, 1972); the scintillation was measured with a standard bialkali photomultiplier through a quartz window and does not include the vacuum ultra-violet (VUV) region.

Secondary photon emission from gases under electron impact has been extensively studied experimentally during the development of the scintillation proportional counters; the process also plays a major role in the photon-induced discharge mechanisms that will be discussed later. Good summaries can be found in numerous review articles (Teyssier *et al*., 1963; Thiess and Miley, 1975; Policarpo, 1977; Policarpo, 1981). In particular, the second reference includes summary tables of

https://doi.org/10.1017/9781009291200.007 Published online by Cambridge University Press

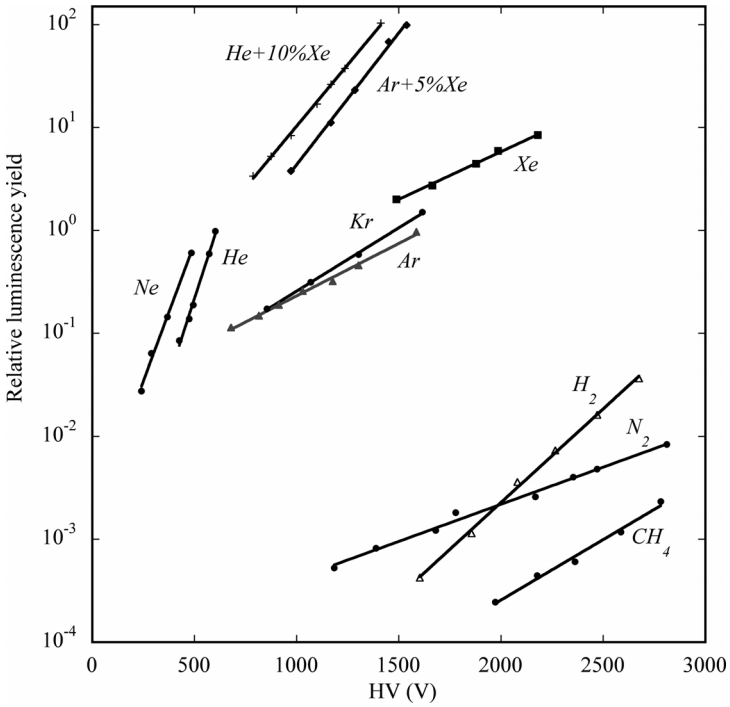

Figure 5.4 Normalized scintillation light yield as a function of field for different gases (Keirim-Markus, 1972). By kind permission of Springer Science+Business Media.

gas mixtures and pressures for which data are available. It is rather unfortunate that most of the measurements have been realized using a thin wire proportional counter, i.e. in a very inhomogeneous electric field; moreover, often only relative emission intensities are given, making difficult any quantitative estimate of the photon yield. Figure 5.5 (Suzuki and Kubota, 1979) shows the secondary scintillation spectra of argon, krypton and xenon measured at atmospheric pressure in a single wire proportional counter at a voltage below threshold for avalanche multiplication. Only the second continuum emission is observed, as noted above, with peaks centred at 128 nm (9.7 eV), 148 nm (8.4 eV) and 170 nm (7.3 eV) for A, Kr and Xe respectively; no emission is observed at longer wavelengths, between 2000 and 6000 Å. It is interesting to compare the emission spectra obtained at low fields with those in gas discharges, see the insets in the figure; Figure 5.6 shows the emission spectrum of krypton for a discharge at 400 torr and for proportional scintillation at 560 torr (Suzuki and Kubota, 1979). In the discharge, that involves the appearance of higher excited states, energetic transitions are possible, leading to emission at visible wavelengths.

https://doi.org/10.1017/9781009291200.007 Published online by Cambridge University Press

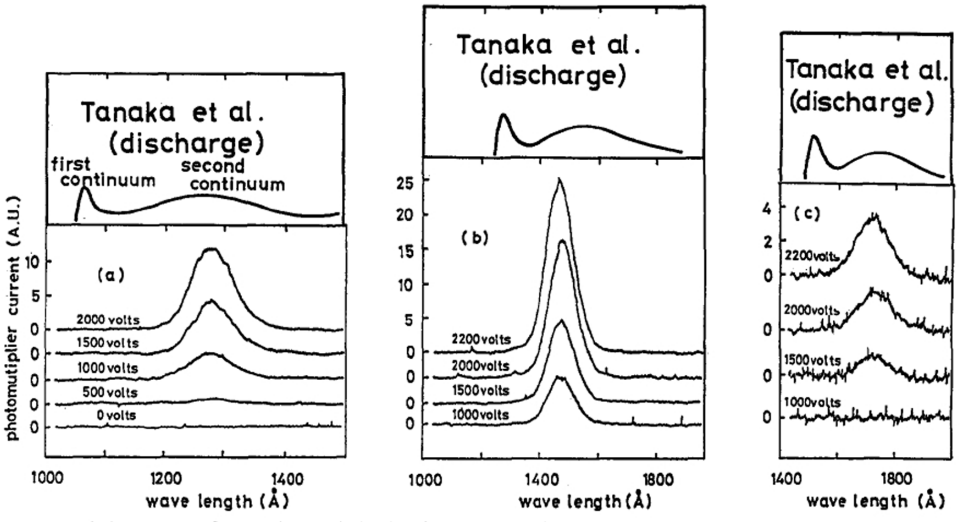

Figure 5.5 Secondary emission spectra of argon (a), krypton (b) and xenon (c) at atmospheric pressure measured with a scintillation proportional counter at different voltages (Suzuki and Kubota, 1979). By kind permission of Elsevier.

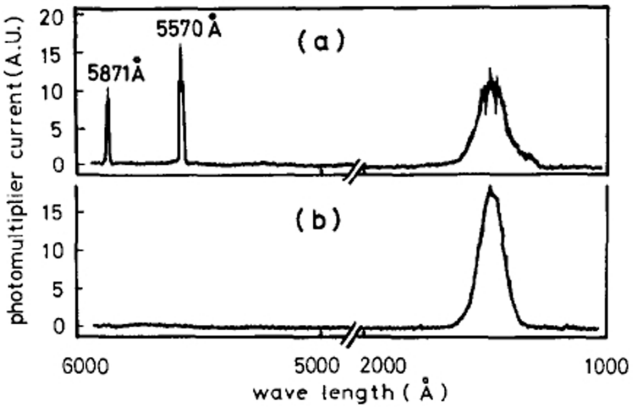

Figure 5.6 Krypton emission spectra at 400 torr in discharge (a) and at 560 torr in the proportional scintillation regime (b) (Suzuki and Kubota, 1979). By kind permission of Elsevier.

Addition to a rare gas of even small amounts of another species with smaller excitation potentials gradually shifts the emission to longer wavelengths, towards that of the additive, as shown in Figure 5.7 and Figure 5.8 for argon–xenon and argon–nitrogen (Takahashi *et al.*, 1983); with nitrogen, the emission occurs in the visible, making it a rather convenient internal wavelength shifter for the use of standard photomultipliers as sensors.

https://doi.org/10.1017/9781009291200.007 Published online by Cambridge University Press

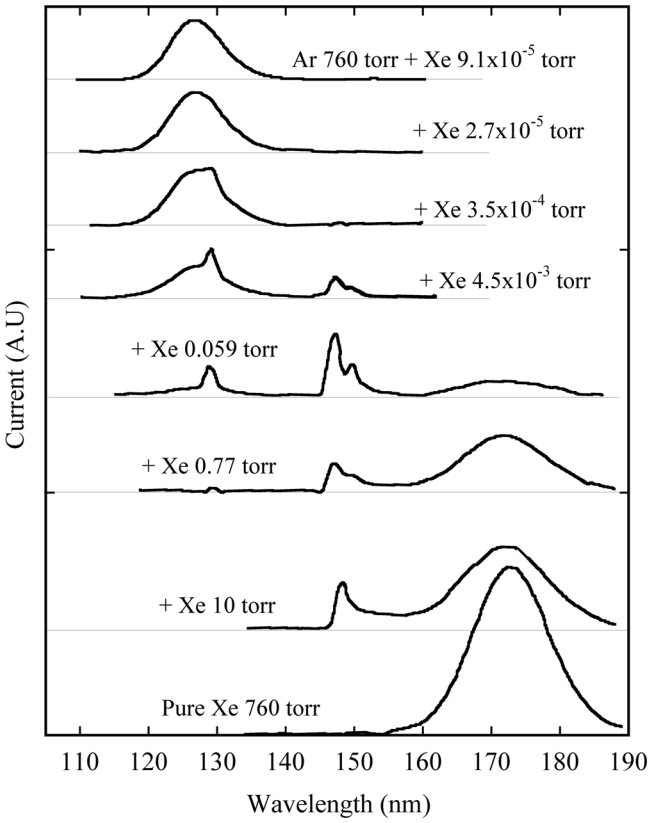

Figure 5.7 Luminescence emission in argon–xenon mixtures (Takahashi *et al.*, 1983). By kind permission of Elsevier.

Addition of molecular species to noble gases strongly reduces these secondary emission effects. In a study aimed at reducing the radiation-induced primary scintillation of nitrogen, harmful in some families of detectors, Morii *et al.* (2004) have measured the primary scintellation photon yield as a function of various additives in N_2; the results for oxygen are shown in Figure 5.9.

Photons emitted by primary or avalanche-induced excitation processes may be absorbed in the gas or by the electrodes; if their energy exceeds the corresponding ionization potentials, they can create secondary electrons adding up to the primary ionization. Depending on the counter geometry and gain, this may result in a spread of the charge, or approach a divergence situation leading to discharges.

Systematic measurements of photon emission by avalanches in heavily quenched proportional counter gas mixtures have been done to provide a quantitative understanding of the secondary photon-mediated processes leading to the appearance of streamers and discharges at high values of the electric field.

https://doi.org/10.1017/9781009291200.007 Published online by Cambridge University Press

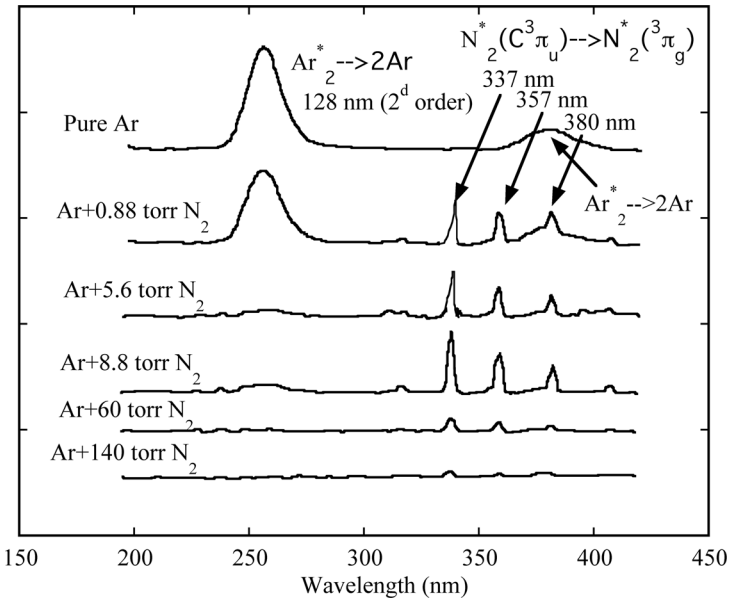

Figure 5.8 Luminescence emission in argon–nitrogen mixtures (Takahashi *et al.*, 1983). By kind permission of Elsevier.

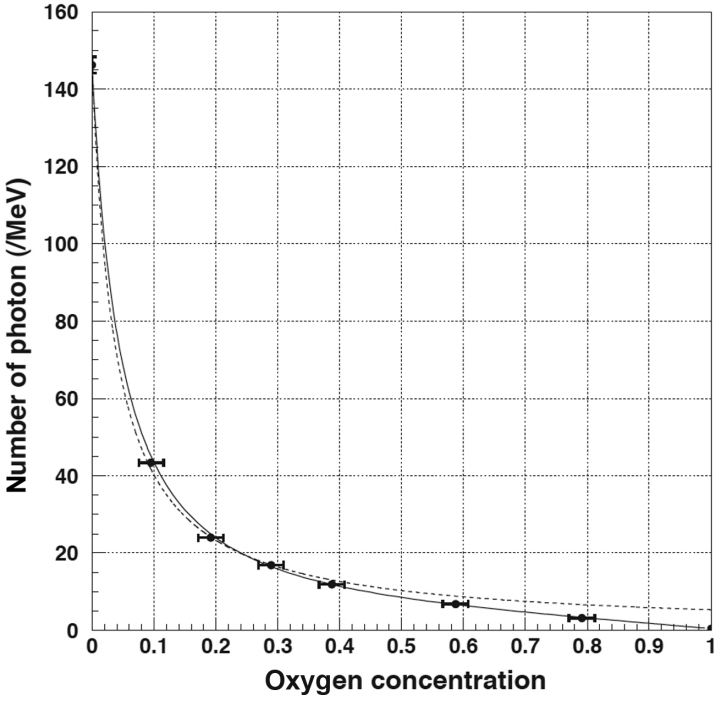

Figure 5.9 Primary scintillation photon yield in nitrogen as a function of oxygen content (Morii *et al.*, 2004). By kind permission of Elsevier.

https://doi.org/10.1017/9781009291200.007 Published online by Cambridge University Press

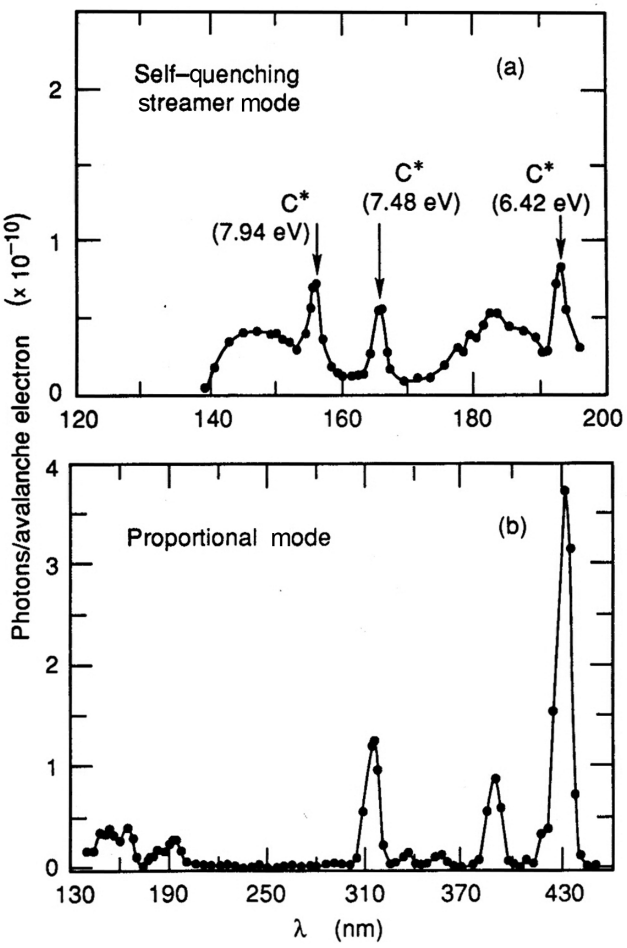

Figure 5.10 Secondary photon yields in argon–methane 90–10 in the SQS and proportional modes (Fraga *et al.*, 1992). By kind permission of Elsevier.

Measured with a single-wire counter coupled to a UV-monochromator, Figure 5.10 and Figure 5.11 show a comparison of emission spectra for argon–methane 90–10 and argon–CO_2 mixtures in the proportional and high gain conditions of the self-quenched streamer (SQS) operation (see Section 7.8); similar measurements are reported for other mixtures, together with attempts to identify the molecular species and excitation levels responsible for the multi-line emissions (Fraga *et al.*, 1992). The photon emission yield in the spectral range of the measurement is normalized to the number of electrons in the avalanche; as can be seen, it is almost two orders of magnitude lower for methane as compared to carbon dioxide, explaining the observed much better photon quenching properties of organic mixtures.

https://doi.org/10.1017/9781009291200.007 Published online by Cambridge University Press

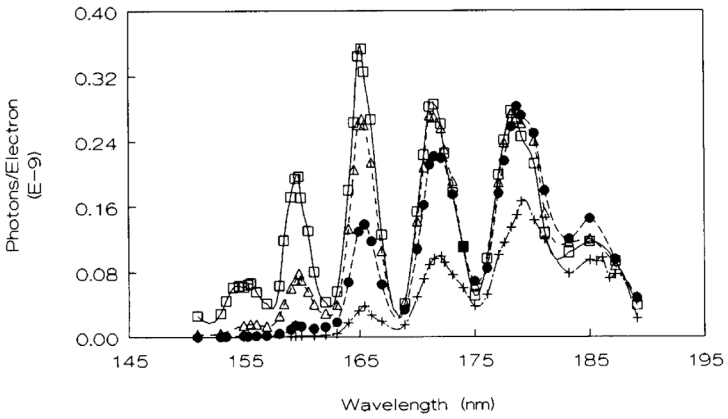

Figure 5.11 Spectral emission of argon–carbon dioxide mixtures in SQS discharges; the CO_2 concentrations vary from 21% (higher peaks) to 100% (lower peaks) (Fraga *et al.*, 1992). By kind permission of Elsevier.

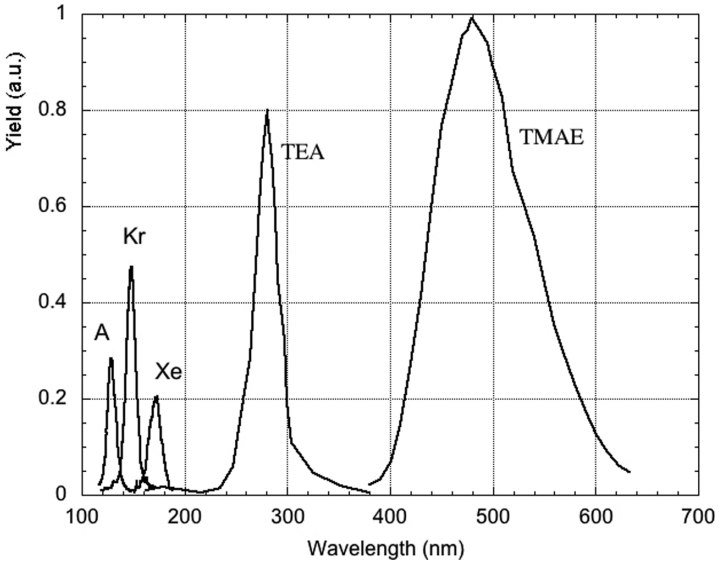

Figure 5.12 Secondary emission spectra of A, Kr, Xe, TEA and TMAE (Breskin *et al.*, 1988). By kind permission of Elsevier.

The fluorescence emission wavelength is longer the lower the excitation potential. Not surprisingly, the vapours used in photosensitive detectors, having low ionization potentials, fluoresce from the near ultra-violet to the visible; Figure 5.12 is a compilation of emission spectra for noble gases and two low-ionization potential vapours, triethyl amine (TEA) and tetrakis dimethyl amino ethylene (TMAE) (Breskin *et al.*, 1988). All spectra have been measured at pressures near

https://doi.org/10.1017/9781009291200.007 Published online by Cambridge University Press

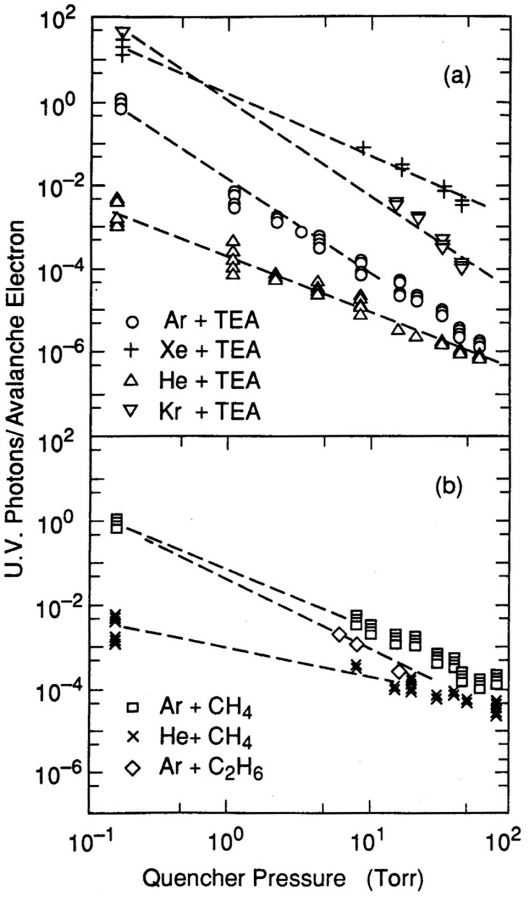

Figure 5.13 High-field secondary photon emission yield for mixtures of noble gases, TEA and some organic quenchers (Fonte *et al.*, 1991). By kind permission of Elsevier.

atmospheric and electric field conditions of charge multiplication. The secondary photon yield in these mixtures is orders of magnitude larger than for standard methane-quenched proportional counter gases, Figure 5.13 (Fonte *et al.*, 1991); due, however, to the longer emission wavelengths, these photons are harmless for the counter itself and are exploited for detection and imaging of radiation with optical means (Chapter 15).

Due to its interest as a fast, non-polymerizing filling in gaseous counters, the photon emission spectra of carbon tetra fluoride (CF_4), pure or in mixtures, have been studied by many authors in various pressure and field conditions (Pansky *et al.*, 1995a; Fraga *et al.*, 2001). As an example, Figure 5.14 (Morozov *et al.*, 2011) shows the scintillation spectrum at 5 bars and for two values of electric field; while the general shape remains the same, the emission at shorter wavelengths is

https://doi.org/10.1017/9781009291200.007 Published online by Cambridge University Press

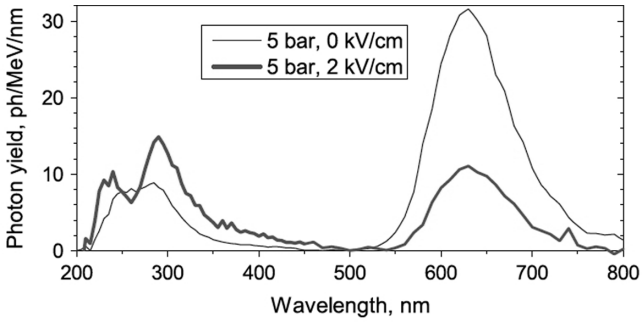

Figure 5.14 Emission spectra of CF_4 at two values of field (Morozov *et al.*, 2011). By kind permission of Elsevier.

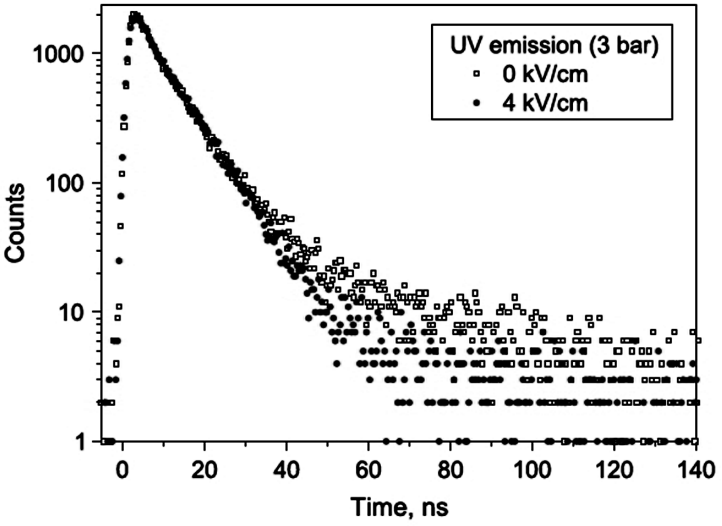

Figure 5.15 CF_4 scintillation decay times at two field values (Morozov *et al.*, 2011). By kind permission of Elsevier.

enhanced at high field. The emission is also rather fast, with typical decay times of a few tens of ns, as shown in Figure 5.15 (Morozov *et al.*, 2011).

Detailed studies of primary scintillation in rare gases show a field-dependent correlation between the primary charge and the luminescence yields induced by ionizing radiation, due to a mechanism of electron–ion recombination (Policarpo *et al.*, 1970; Suzuki, 1983; Saito *et al.*, 2008); Figure 5.16, from the second reference, shows the relative light and charge yield measured as a function of reduced electric field for argon, krypton and xenon. A simultaneous measurement of the two quantities can be exploited to improve the energy resolution of counters (Bolotnikov and Ramsey, 1999).

https://doi.org/10.1017/9781009291200.007 Published online by Cambridge University Press

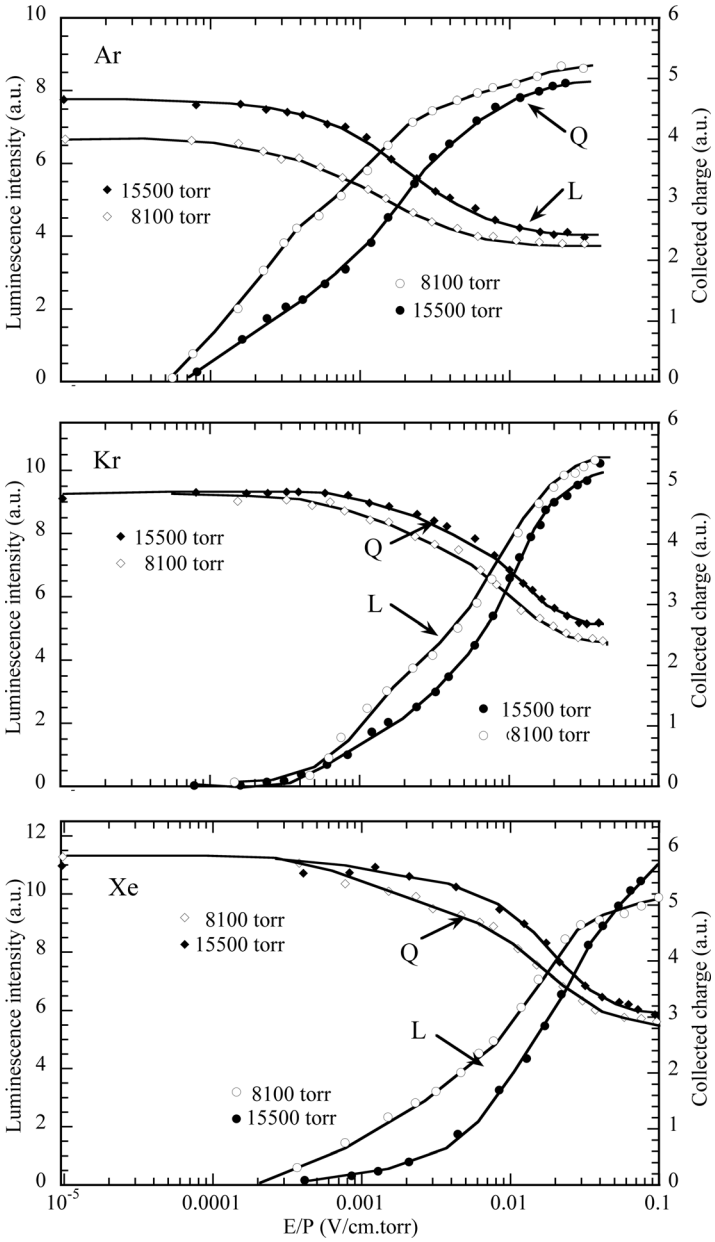

Figure 5.16 Luminescence (L) and charge yield (Q) in rare gases as a function of electric field (Suzuki, 1983). By kind permission of Elsevier.

Primary scintillation from liquid noble gases has a high photon yield and fast decay, and has been studied extensively in view of applications for gamma ray calorimetry, rare event and dark matter searches (Aprile *et al.*, 2002); as the emission is in the far and vacuum ultra-violet, appropriate wavelength shifters or

https://doi.org/10.1017/9781009291200.007 Published online by Cambridge University Press

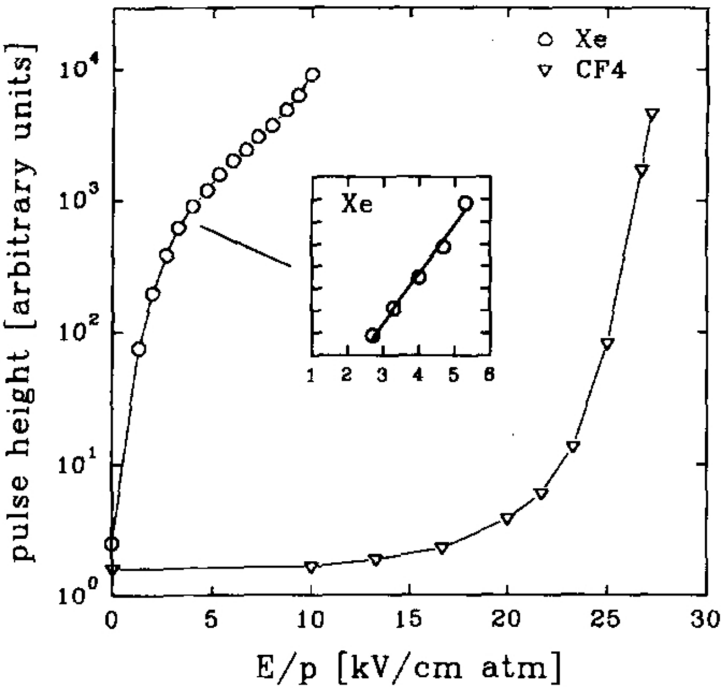

Figure 5.17 Relative scintillation yield of xenon and carbon tetrafluoride as a function of electric field. For CF_4, no secondary photon enhancement is observed before charge multiplication (Pansky *et al.*, 1995). By kind permission of Elsevier.

internal CsI photosensitive layers have to be used for detection. A summary of results for pure liquid rare gases and their mixtures and can be found in Doke and Masuda (1999).

Motivated by the problems connected to the primary photon emission from carbon tetrafluoride-filled radiators in Cherenkov counters, the scintillation yield of CF_4 in the UV region has been measured and compared with that of xenon, Figure 5.17 (Panski *et al.*, 1995).

5.3 Ionization and charge multiplication

When the energy of the electron accelerated by the electric field exceeds the ionization potential of the atom or molecule, bound electrons can be ejected, leaving behind a positive ion. Depending on the energy transfers involved and on the charge density, multiple ionized states can be produced, although in the conditions normally met in proportional counters, with electron energies below a few tens of eV, the creation of singly charged ions is the most likely process.

https://doi.org/10.1017/9781009291200.007 Published online by Cambridge University Press

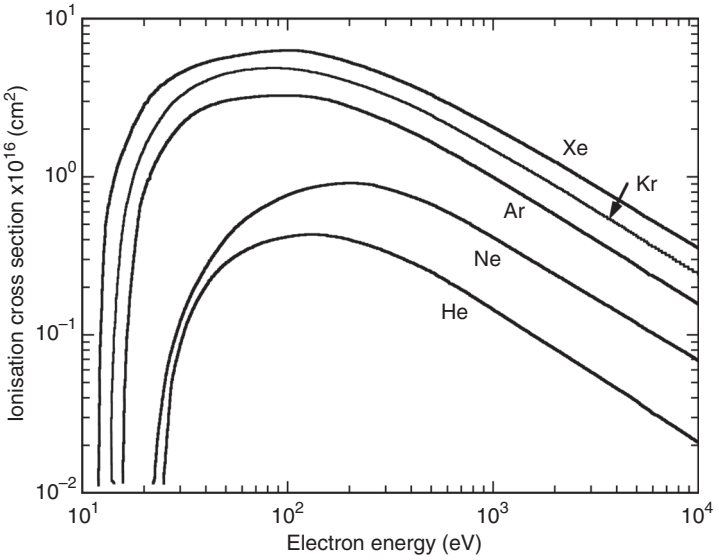

Figure 5.18 Ionization cross sections of noble gases as a function of electron energy. Simplified plot from data in Rapp and Englander-Golden (1965).

If not lost by capture or absorption in the walls, primary and secondary electrons continue their path, and can further ionize the gas molecules. The ionization cross section increases rapidly above the threshold and for most gases has a maximum at an energy above 100 eV, as shown in Figure 5.18 (Rapp and Englander-Golden, 1965).

The mean free path for ionization λ is defined as the average distance an electron has to travel before having an ionizing collision; its inverse, $\alpha = \lambda^{-1}$, is the ionization or first Townsend coefficient, and represents the number of ion pairs produced per unit length of drift; it relates to the ionization cross section through the expression:

$$\alpha = N\,\sigma_{\mathrm{i}}, \tag{5.1}$$

where N is the number of molecules per unit volume.

As for other quantities in gaseous electronics, the Townsend coefficient is proportional to the gas density and therefore to the pressure P; the ratio α/P is a sole function of the reduced field E/P, as shown in Figure 5.19 for noble gases (Druyvesteyn and Penning, 1940).

Addition to a pure noble gas of even small quantities of a different species not only modifies the energy distribution of electrons, but can also open new channels for radiative and ionizing transitions. If the ionization potential of one species is lower than the excitation potential of the other, a very effective process of

https://doi.org/10.1017/9781009291200.007 Published online by Cambridge University Press

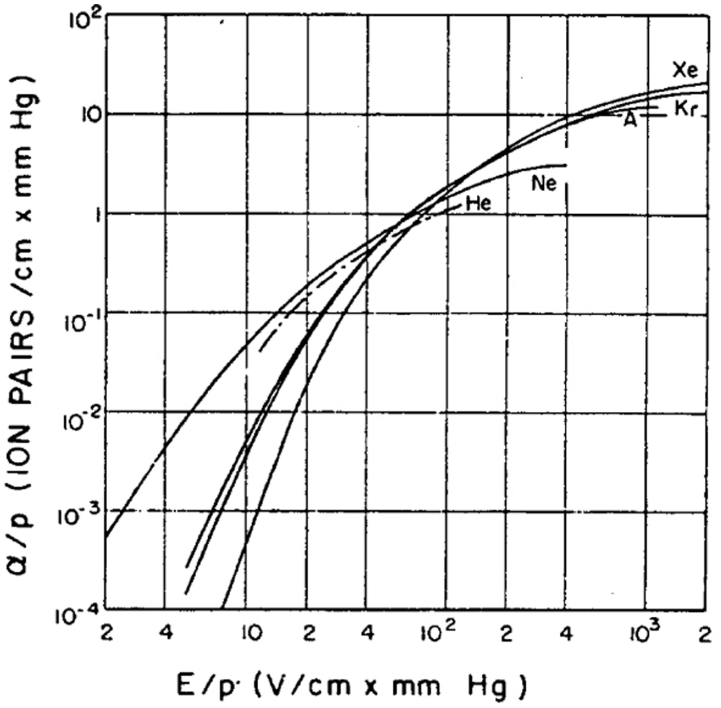

Figure 5.19 First Townsend coefficient as a function of field for the rare gases (Druyvesteyn and Penning, 1940) By kind permission of the American Physical Society.

collisional transfer can take place, resulting in the increase of ionized states (Penning effect):

$$A^* + B \rightarrow A + B^+ + e.$$

A well-known illustration of this effect results from the addition of small fractions of argon ($E_i = 15.8$ eV) to neon ($E_x = 16.6$ eV), that leads to a very effective increase of the ionization yield as compared to its value for both argon and neon alone, Figure 5.20 (Druyvesteyn and Penning, 1940). Penning mixtures are widely used in proportional counters to improve their energy resolution (Sipilå, 1976).

The process of successive ionizations by collision results in charge amplification in proportional counters. Consider an electron released in a region of uniform electric field. After a mean free path $1/\alpha$, one electron–ion pair will be produced, and the two electrons continue their drift generating, after another mean free path, two more ion pairs and so on. If n is the number of electrons in a given position, the increase in their number after a path dx is d$n = n\,\alpha$dx; integrating over a path length x:

$$n = n_0 e^{\alpha x} \text{ or } M = \frac{n}{n_0} = e^{\alpha x}, \tag{5.2}$$

https://doi.org/10.1017/9781009291200.007 Published online by Cambridge University Press

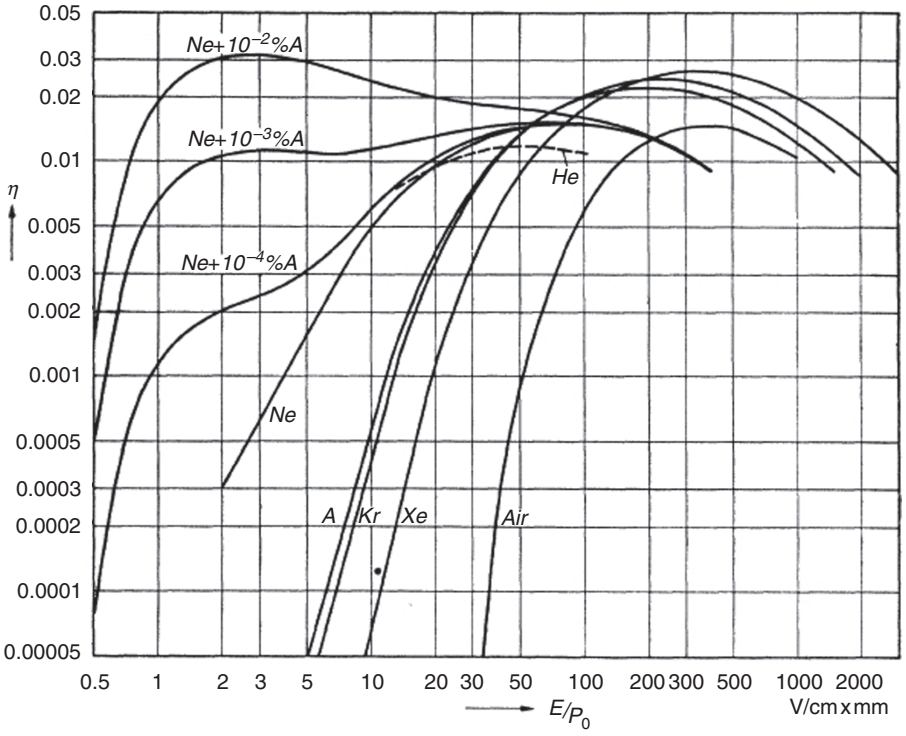

Figure 5.20 Ionization coefficient in rare gases and mixtures, illustrating the Penning effect (Druyvesteyn and Penning, 1940). By kind permission of the American Physical Society.

where M represents the charge multiplication factor. In the more general case of a non-uniform electric field, $\alpha = \alpha(x)$, the expression has to be modified as follows:

$$M = \mathrm{e}^{\int_{x_1}^{x_2} \alpha(x)\mathrm{d}x}, \tag{5.3}$$

where x_1 and x_2 are the initial and final coordinates of the multiplication path. Due to the very large difference in mobility and diffusion of electrons and ions, discussed in the previous chapter, the process of charge multiplication results in a characteristic drop-like charge distribution, or avalanche, with all electrons at the front and a slow ions trail.

The multiplication factor for arbitrary field geometry can be computed by knowing the dependence of the Townsend coefficient on the electric field. Several analytic expressions exist for α, valid in different regions of E; for a summary see for example Palladino and Sadoulet (1975). A simple approximation, due to Korff (1955) is given by:

https://doi.org/10.1017/9781009291200.007 Published online by Cambridge University Press

Table 5.2 *Parameters in Korff's expressions.*

Gas	A ($cm^{-1}torr$)	B ($V\ cm^{-1}torr^{-1}$)	k (cm^2V^{-1})
He	3	34	0.11×10^{-17}
Ne	4	100	0.14×10^{-17}
Ar	14	180	1.81×10^{-17}
Xe	26	350	
CO_2	20	466	

$$\frac{\alpha}{P} = Ae^{-\frac{BP}{E}}, \tag{5.4}$$

where A and B are phenomenological constants whose approximate values are given in Table 5.2 for several gases (Korff, 1955). In the same field region, the coefficient can be assumed to be proportional to the average electron energy:

$$\alpha = kN\varepsilon. \tag{5.5}$$

Useful for qualitative considerations, the double exponential dependence of α on the field may induce large errors in the estimate even for small differences in the value of the parameters used.

With the opening of the new channels of interaction, the shape of the energy distribution is also substantially modified. With proper parameterization of the contributing cross sections, the transport theory outlined in the previous chapter can be extended to cover the high field inelastic phenomena. In Figure 5.21, experimental data for argon (Kruithof and Penning, 1937; Jelenak *et al.*, 1993) are compared with Korff's approximation, and the predictions of the program MAGBOLTZ (Biagi and Veenhof, 1995b).

Figure 5.22 provides the values computed for pure argon, methane and a 90–10 mixture of the two, at NTP. One can see that the field required to obtain a given value of α is about twice as large in methane than in argon, a clear consequence of the electron 'cooling' effect of molecular gases. The computed ionization coefficients in other gases at NTP are given in Figure 5.23.

The ionization coefficients can be measured using an ionization chamber with a parallel plate multiplication structure; Figure 5.24 is an example of measured values for argon–isobutane mixtures at NTP (Sharma and Sauli, 1992).

The MAGBOLTZ program can be used also to estimate the dependence of the multiplication factor on pressure and temperature. The computed gain variation for a 70–30 argon–carbon dioxide mixture as a function of the ratio *T/P* shows a good agreement with measurements, Figure 5.25 (Altunbas *et al.*, 2003). At constant temperature, a 1% pressure increase results in a gain reduction of about 10%, a parameter to take in due consideration when designing or operating gaseous detectors.

https://doi.org/10.1017/9781009291200.007 Published online by Cambridge University Press

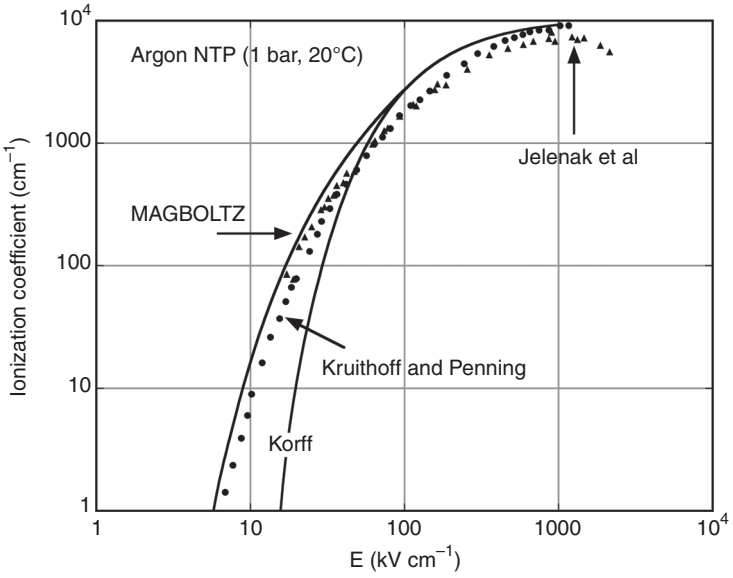

Figure 5.21 Comparison between experimental data of the Townsend coefficient for argon, full points (Kruithoff and Penning, 1937; Jelenak *et al*., 1993), Korff's approximation (Korff, 1955) and MAGBOLTZ calculation by the author.

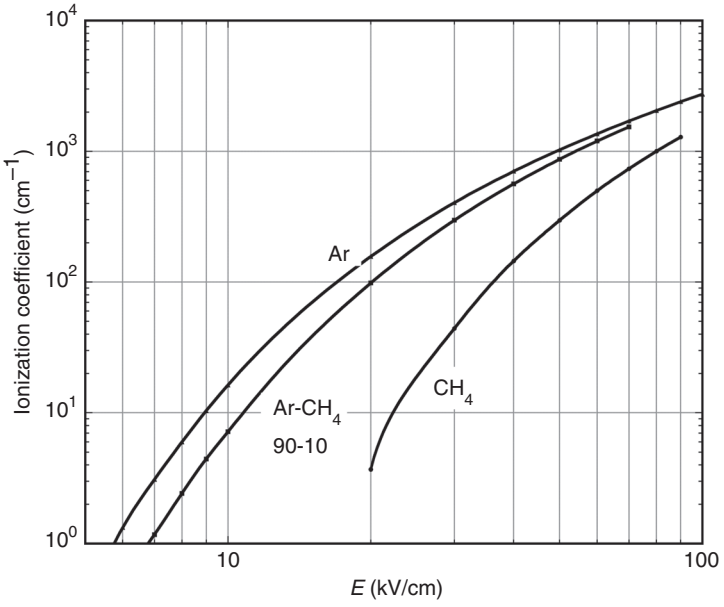

Figure 5.22 Computed Townsend coefficient for argon, methane and their mixture (NTP).

https://doi.org/10.1017/9781009291200.007 Published online by Cambridge University Press

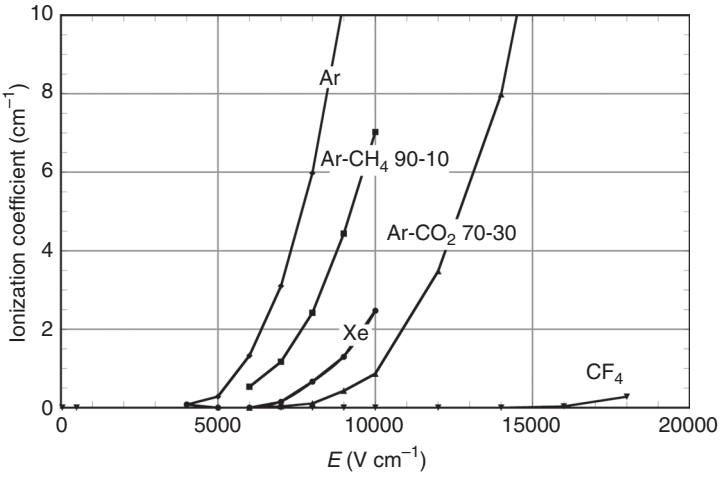

Figure 5.23 Computed Townsend coefficient for several pure gases and mixtures at NTP.

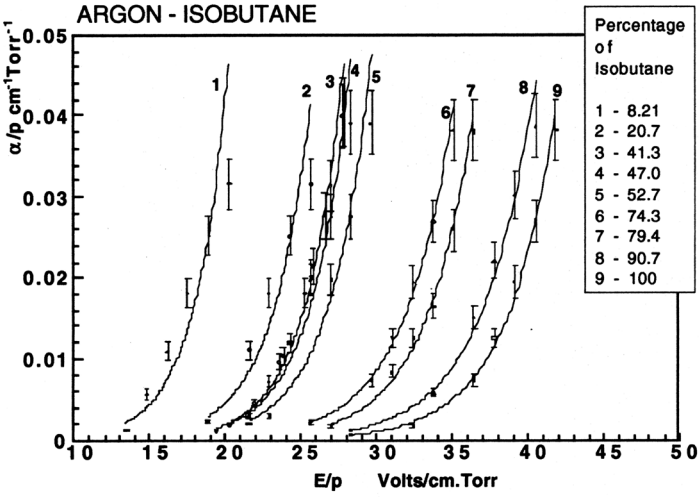

Figure 5.24 Experimental measurements of the Townsend coefficient for argon–isobutane mixtures (Sharma and Sauli, 1992). By kind permission of Elsevier.

5.4 Avalanche statistics

The considerations in the previous section refer to the average avalanche development in uniform fields, described by the Townsend coefficient α. However, statistical variations in the individual ionizing collisions paths during the avalanche development generate dispersions around the average. The problem of avalanche fluctuations has been extensively studied in the early developments of the gaseous

https://doi.org/10.1017/9781009291200.007 Published online by Cambridge University Press

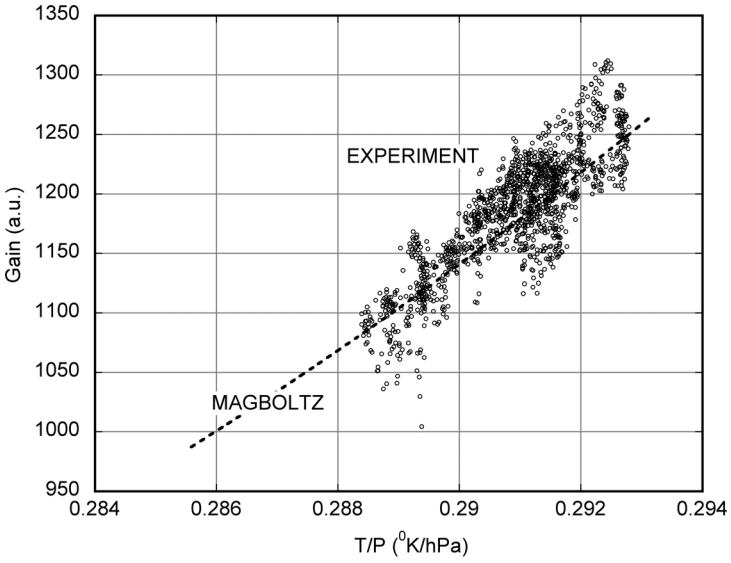

Figure 5.25 Dependence of multiplication factor on T/P in Ar-CO_2 70–30 (Altunbas *et al.*, 2003). By kind permission of Elsevier.

counters, since it contributes to their intrinsic energy resolution. For an avalanche initiated by a single electron, one needs to estimate the avalanche size distribution, i.e. the probability $P(n, s)$ that there are exactly n electrons in the avalanche after a path s; this is easily done for uniform fields, and can be extended to other configurations by proper averaging (Byrne, 2002). Given the value of α, the probability that an electron does not experience multiplication after a path s is:

$$P(1, s) = \mathrm{e}^{-\alpha s};$$

the probability that there is one, and only one, ionizing collision (two electrons present after a path x) can then be written as:

$$P(2, s) = \mathrm{e}^{-\alpha s}(1 - \mathrm{e}^{-\alpha s});$$

and, in general, to have n and only n electrons:

$$P(n, s) = \mathrm{e}^{-\alpha s}(1 - \mathrm{e}^{-\alpha s})^{n-1},$$

defining $\overline{n} = \mathrm{e}^{\alpha s}$ as the average number of electrons in the avalanche (average avalanche size):

$$P(n, s) = \frac{1}{\overline{n}}\left(1 - \frac{1}{\overline{n}}\right)^{n-1} \approx \frac{\mathrm{e}^{-n/\overline{n}}}{\overline{n}}, \tag{5.6}$$

the approximation, corresponding to the first term in a series expansion of the exponential, is valid for $\overline{n} \gg 1$ and is often referred to as Furry's law. The

https://doi.org/10.1017/9781009291200.007 Published online by Cambridge University Press

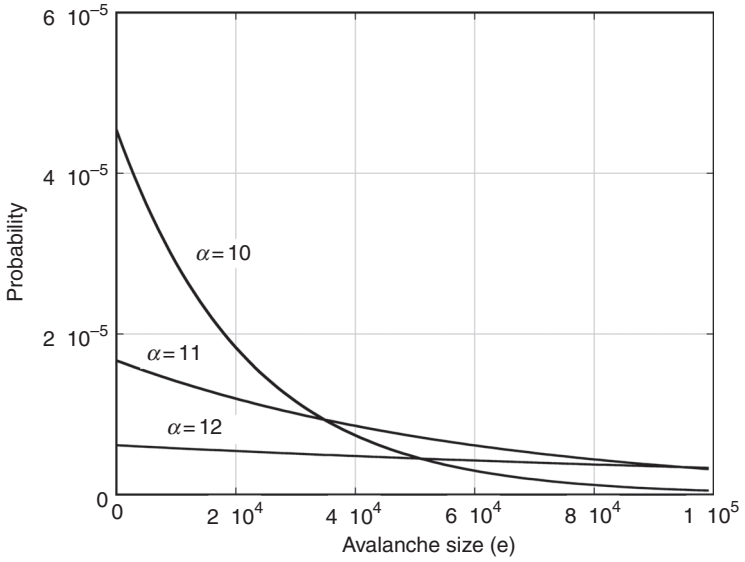

Figure 5.26 Avalanche size probability for several values of the Townsend coefficient.

probability has the particularity to decrease exponentially from a maximum at $n = 1$; surprisingly, the highest probability is for electrons to not multiply at all over the gap. The mean and the variance of the distribution are equal to the average avalanche size $\overline{n}$; the distribution does not depend explicitly on the gap thickness s (although the average size does). Figure 5.26 shows the computed avalanche size distribution in a unit length gap for three values of average size.

For an avalanche starting with N initial electrons, the corresponding size distribution can be obtained as a convolution of N independent exponentials (Breyer, 1973):

$$P(n,N) = \frac{1}{\overline{n}} \left(\frac{n}{\overline{n}}\right)^{N-1} \frac{\mathrm{e}^{-\frac{n}{\overline{n}}}}{(N-1)!}, \tag{5.7}$$

where $\overline{n}$ is the average avalanche size for one electron. The expression reduces to (5.4) for $N = 1$, and is functionally identical to a Poisson distribution in the parameter $n/\overline{n}$. The average avalanche size, obtained by integration of the expression, is of course $N\,\overline{n}$.

In Figure 5.27, computed avalanche size distributions are shown for equal gain at increasing values of N. For a large number of primary multiplying electrons ($>\sim$10) the distributions tend to have a Gaussian shape centred around the average total charge $N\,\mathrm{e}^{\alpha s}$ and with a variance $\sqrt{N}$, independently of the gain; the same

https://doi.org/10.1017/9781009291200.007 Published online by Cambridge University Press

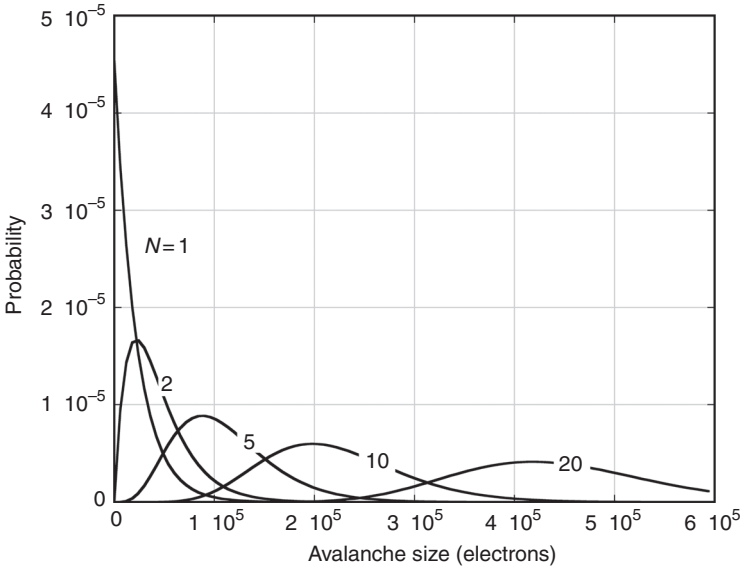

Figure 5.27 Avalanche size probability distributions for increasing values of the number of primary electrons.

property holds for the corresponding Poisson distribution for large values of the parameter in the exponential.

Expression (5.7) can be conveniently rewritten and renormalized as a function of the reduced variable $x = n/\overline{n}$:

$$P(x, N) = \frac{x^{N-1}}{(N-1)!} \mathrm{e}^{-x}. \tag{5.8}$$

Figure 5.28 shows the renormalized function computed for several values of N; for $N = 10$, a Gaussian distribution with average $N\,\overline{n}$ and variance $\sqrt{N}$ is also plotted for comparison.

It has been observed experimentally that the single electron avalanche distribution can evolve from a pure exponential into a peaked shape at very high values of gain. First described by Curran (Curran and Craggs, 1949), the appearance of a peak in the distribution was theoretically analysed by many authors. Considering that for large gains, and therefore small values of the mean ionization length, the electrons use a non-negligible part of their path to acquire a sufficient energy to ionize, one can deduce the following general expression (also named the Polya distribution) for the single electron avalanche size probability (Byrne, 1969):

$$P(x, \theta) = [x(\theta + 1)]^{\theta} \mathrm{e}^{-x(\theta+1)}, \tag{5.9}$$

https://doi.org/10.1017/9781009291200.007 Published online by Cambridge University Press

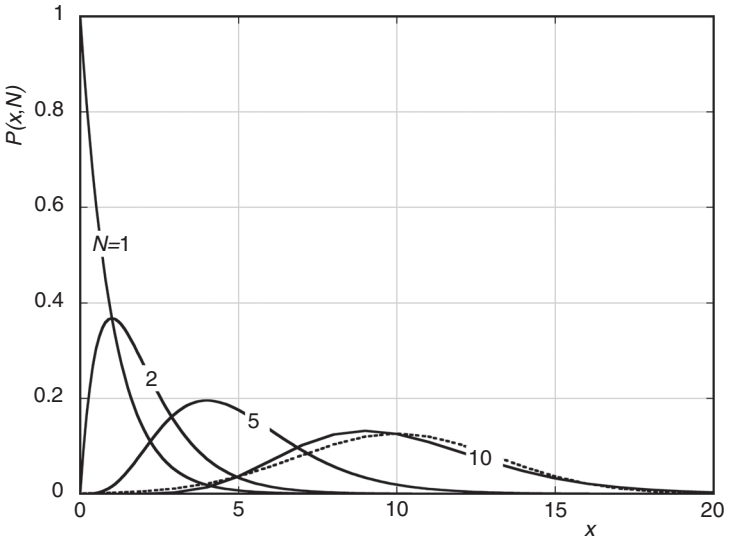

Figure 5.28 Normalized avalanche size probability. The dashed curve is a Gaussian distribution for $N = 10$.

where $x = n/\overline{n}$ is the number of electrons in the avalanche, with average value $\overline{n}$, and θ a parameter; for $\theta = 0$ the expression reduces to the simple exponential (5.6); Figure 5.29 shows the distributions for several values of θ.

Figure 5.30 is an experimental verification of the transition of the single-electron avalanche size distribution from exponential to a peaked Polya shape at increasing values of fields, measured with a methylal-filled counter (Schlumbohm, 1958).

Strictly valid only for the avalanche development in uniform fields, the Polya formulation is widely used to describe measurements obtained with proportional counters and other non-uniform field structures.

Avalanche and gas gain fluctuations can be assessed using Monte Carlo calculations based on the MAGBOLTZ program described in the previous section; the flexibility and wide data base of the program permits one to compare performances of different detector geometry and gas filling (Schindler *et al.*, 2010).

5.5 Streamer formation and breakdown

The multiplication factor cannot be increased at will. Secondary ionization processes in the gas and on the walls produced by photons emitted in the primary avalanche spread the charge over the gas volume; the space charge-induced distortions of the electric field, strongly increasing in front of and behind the

https://doi.org/10.1017/9781009291200.007 Published online by Cambridge University Press

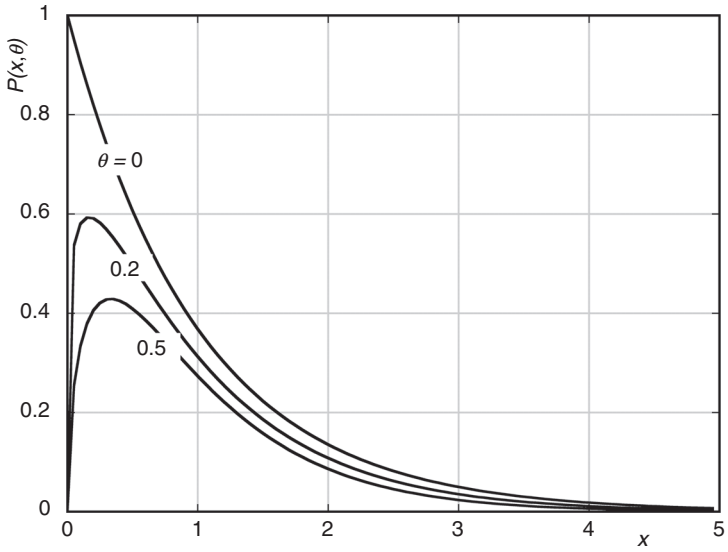

Figure 5.29 Polya single-electron avalanche size probability for several values of the parameter θ.

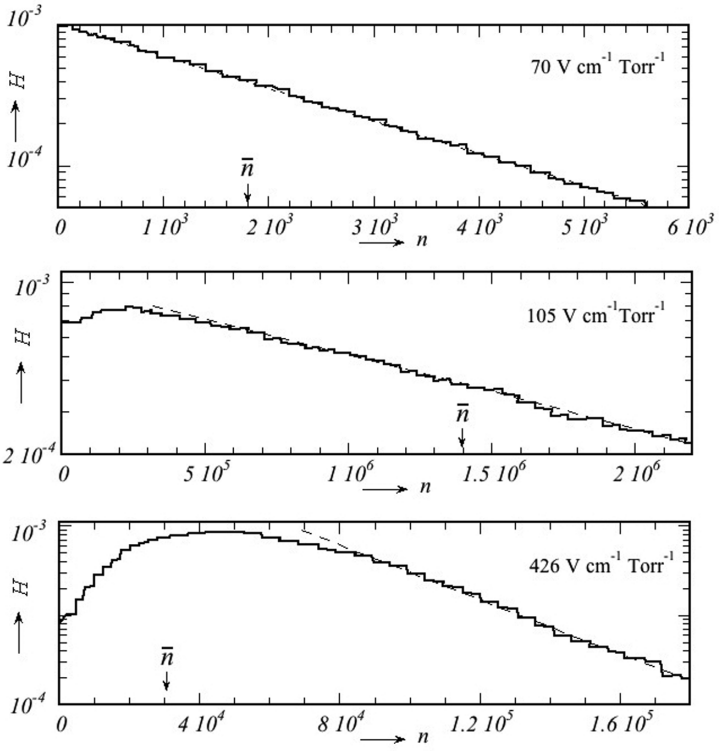

Figure 5.30 Evolution of the avalanche size from exponential to a Polya distribution at increasing values of field (Schlumbohm, 1958). By kind permission of Springer Science+Business Media.

https://doi.org/10.1017/9781009291200.007 Published online by Cambridge University Press

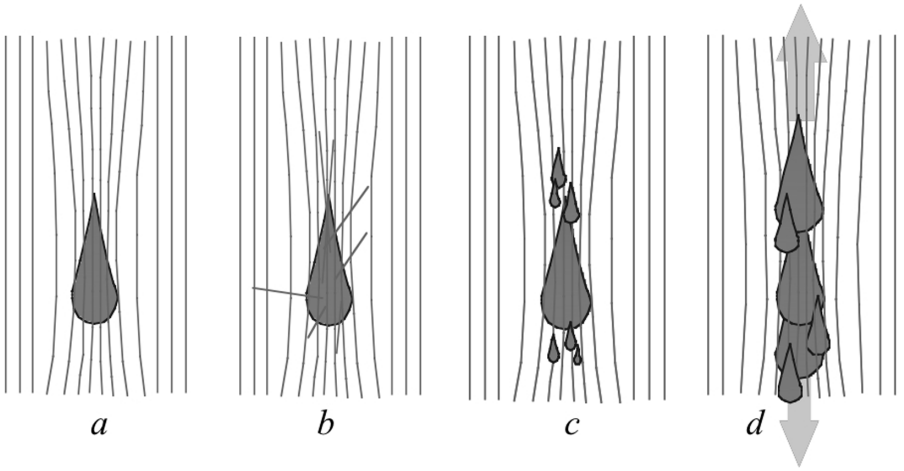

Figure 5.31 Schematic representation of the transition from avalanche to streamer.

multiplying charge, enhance the formation of secondary avalanches and may cause the transition of the proportional avalanche to a streamer and eventually to a spark breakdown. A qualitative description of the main processes leading to the avalanche–streamer transition is shown in Figure 5.31. At the onset of charge multiplication, the high density of ions and electrons in the avalanche modify the original electric field, increasing it in front of and behind the avalanche (*a*); photons emitted isotropically from inelastic collisions in the avalanche front create secondary electrons by photo-ionization of the gas molecules (*b*). Secondary avalanches then develop from electrons created in the regions of higher field (*c*) and the process continues with a forward and backward propagation of the charges, starting a streamer (*d*).

If not damped by the detector geometry or by a reduction of field, the streamer can propagate through the whole gas gap, leading to a spark breakdown. A phenomenological limit to the proportional avalanche multiplication before the transition is given by the empirical condition (Raether's limit):

$$\alpha x < 20, \tag{5.10}$$

or a total avalanche size, product of initial ionization and gain, of around 10^8. However, the statistical distribution of the energy of electrons, and therefore of the gain, generally does not allow one to operate gaseous counters at average gains above around 10^6 to avoid breakdowns.

The conditions and outcomes of the streamer transition have been extensively studied and are described in many textbooks (Meek and Cragg, 1953; Loeb, 1961;

https://doi.org/10.1017/9781009291200.007 Published online by Cambridge University Press

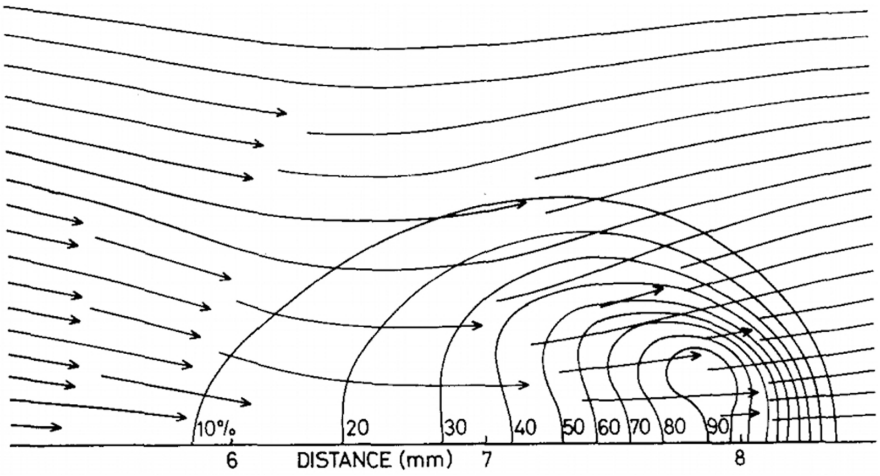

Figure 5.32 Two-dimensional plot of the electron density and electric field near the end of the avalanche development process (Evans, 1969). By kind permission of Elsevier.

Raether, 1964). More recently, in the course of the development of the gaseous detector, terms describing short-distance photo-ionization have been included in the transport equations for the atomic species involved, leading to numerical solutions of the streamer and breakdown transition (Evans, 1969; Fonte, 1996). Figure 5.32 and Figure 5.33, from the first reference, show a two-dimensional map of the electron charge distribution and the field at a certain point of the avalanche development, and respectively the longitudinal distribution of electron density and axial field at successive times. The field enhancements in the front and back of the avalanche are visible, as well as the reduction within the avalanche itself due to the high density of ions and electrons.

The presence of a precursor, a fast and short pulse induced by the streamer transition before the main signal of the full discharge, described by Raether, has been observed by several authors and is well reproduced by the breakdown simulation model (Fonte *et al.*, 1991; Anderson *et al.*, 1994). The precursor provides in fact the faster signal after the ionizing encounter, and is exploited in detectors providing the best time resolutions (see Chapter 12).

For high events rates, the accumulation of charges results in a rate-dependent reduction of maximum gain, the invariant being the total charge of the avalanche, as seen in Figure 5.35, providing the maximum event rate before breakdown for several values of the avalanche size (Fonte *et al.*, 1999). The measurements were realized with parallel plate chambers having different electrode resistivity; the solid

https://doi.org/10.1017/9781009291200.007 Published online by Cambridge University Press

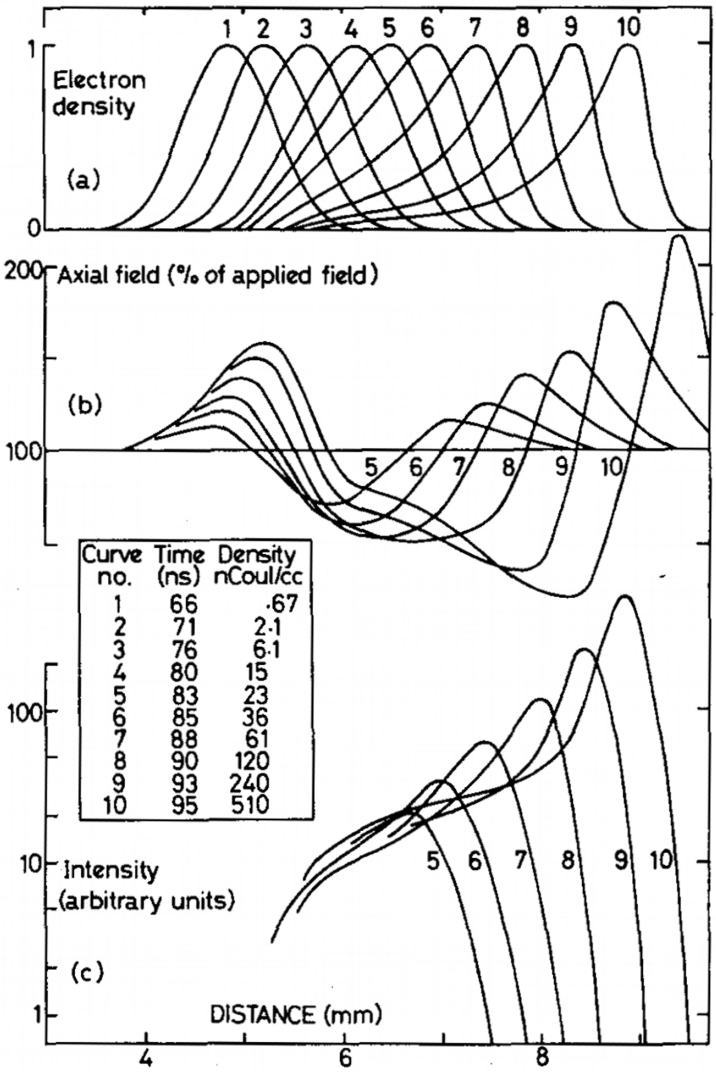

Figure 5.33 Computed axial distributions of electron density (a) and field (b) at ten successive positions in the avalanche propagation. The relative intensity of photon emission is given in (c) (Evans, 1969). By kind permission of Elsevier.

black line is the so-called metallic limit, corresponding to the use of conductive electrodes.

A naive calculation assuming typical values for the avalanche size (~1 mm^2) and a positive ion clearing time for a small gap, high field device (~1 μs) suggests that the probability of two avalanches overlapping in time at a flux of 10^5 Hz/mm^2 is only 10%, making obscure the observed collective effect. A more rigorous calculation, however, taking into account the statistical fluctuations in the

https://doi.org/10.1017/9781009291200.007 Published online by Cambridge University Press

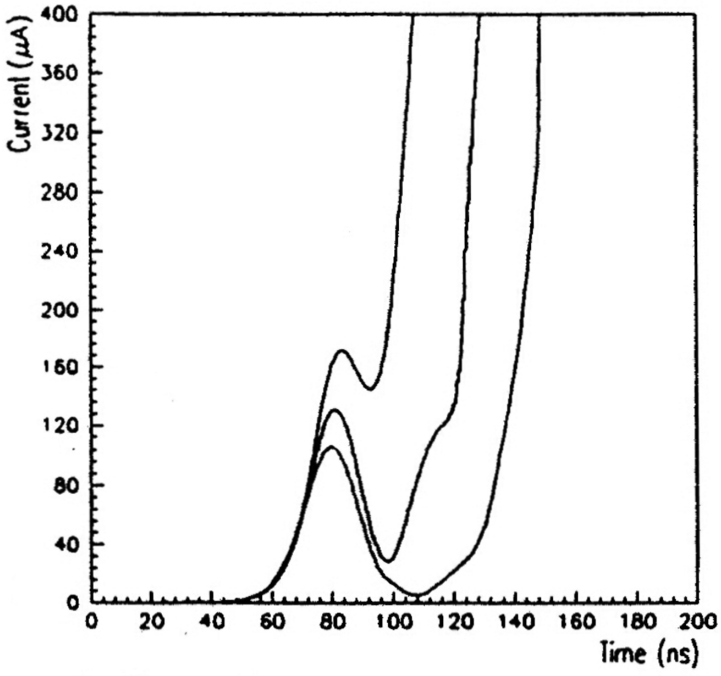

Figure 5.34 Model simulation of the signals at the streamer transition, with fast discharge precursors at increasing gains (Fonte *et al.*, 1991). By kind permission of Elsevier.

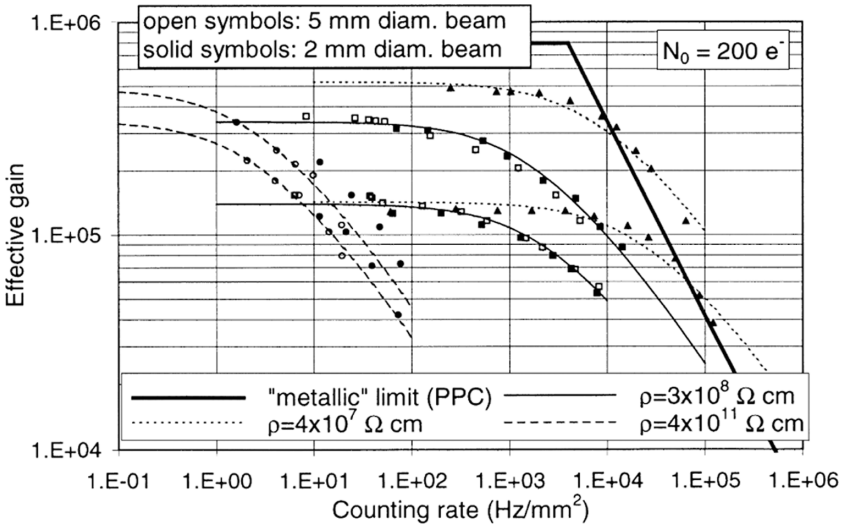

Figure 5.35 Effective gain of parallel plate counters as a function of counting rate (Fonte *et al.*, 1999). By kind permission of Elsevier.

https://doi.org/10.1017/9781009291200.007 Published online by Cambridge University Press

avalanche size, reproduces rather well the observed gain–rate dependence (Peskov and Fonte, 2009).

The mechanisms, outcomes and methods of prevention of discharges in parallel plate counters have been extensively studied in the course of the development of resistive plate chambers, and are discussed in the Chapter 12, dedicated to this family of detectors.

https://doi.org/10.1017/9781009291200.007 Published online by Cambridge University Press